Biosensors and Bioelectronics 306 (2026) 118682

Contents lists available at ScienceDirect

Biosensors and Bioelectronics

journal homepage: www.elsevier.com/locate/bios

Living electronics: Coupling *S. oneidensis* MtrC-SpyTag cells to SpyCatcher-functionalized electrodes for direct electron transfer

Lukas Kneuer [a], René Wurst [a], Christian Jonas Lapp [a], Nhật Quang Lê [a], Leah Kobza [a,1], Milena Menzel [a,2], Edina Marlen Klein [a,3], Laura-Alina Philipp [a], Catarina M. Paquete [b], Johannes Gescher [a,*]

[a] Institute of Technical Microbiology, Hamburg University of Technology, Hamburg, Germany
[b] Instituto de Tecnologia Química e Biológica António Xavier, Universidade Nova de Lisboa, Oeiras, Portugal

ARTICLE INFO

Keywords:
MtrC
SpyTag/catcher
Shewanella oneidensis
Direct electron transfer

ABSTRACT

This work set out to establish an easily applicable system to improve a broad range of bioelectronic devices using the SpyTag-SpyCatcher crosslinking system together with one of the model organisms for extracellular electron transport, *Shewanella oneidensis*. Therefore, the surface-displayed *c*-type cytochrome MtrC was equipped with an accessible SpyTag and coupled to SpyCatcher-functionalized surfaces. A transposon screen followed by nanopore sequencing was conducted in order to identify integration positions which facilitate MtrC functionality while the SpyTag is surface accessible. Three integration positions (W314, Y417, T603) were chosen for further characterization. Expression of the MtrC-SpyTag constructs in a *S. oneidensis* strain lacking all outer membrane cytochromes restored the ability to reduce an extracellular electron acceptor. Two of the three strains reached reduction rates at the wildtype MtrC level proving that the integrated SpyTag does not hamper extracellular electron transfer. *In vivo,* all three constructs showed significantly better binding properties to SpyCatcher functionalized magnetic beads than the wildtype MtrC control. The two most promising candidates were coupled to conductive, magnetic gold nanoparticles and directed towards a screen-printed electrode showcasing how MtrC-SpyTag expression can improve bioelectronic devices. A significantly higher charge transfer compared to the wildtype control was reached in linear sweep voltammetry and chronoamperometry experiments. Moreover, a shift towards direct electron transfer was observed which reduces the problem of redox shuttle washout in flowthrough systems. Direct binding of the cells to SpyCatcher functionalized electrodes enabled robust current production even after thorough washing of the electrodes while control cells failed to produce current under these conditions. The versatile SpyCatcher toolbox can be used together with the here reported strains to eliminate bottlenecks in bioelectronics like poor biofilm formation or the production of an insulating extracellular polymer matrix.

1. Introduction

The rapid advancements in the electronics industry and nanotechnology have led to an increased demand for conductive materials, particularly for flexible wearable devices and innovations on the Internet of Things (Rogers et al., 2010; Someya et al., 2016). Currently, most electronic products rely on rigid materials that often contain rare or expensive elements (Gao et al., 2024). These materials can be difficult to recycle and may pose health risks due to the presence of heavy metals or hazardous chemicals (Kiddee et al., 2013). Therefore, it is essential to identify sustainable alternatives that not only maintain high performance but also introduce beneficial new characteristics. Additionally, there is a growing interest in interfacing electronics with biological entities, which has given rise to the field of bioelectronics. The primary goal is to connect biological materials with electronics and utilize these hybrid materials to influence biological functions, detect specific

* Corresponding author.
E-mail address: johannes.gescher@tuhh.de (J. Gescher).
[1] EUROIMMUN Medizinische Labordiagnostika AG, Selmsdorf, Germany.
[2] University of Applied Sciences Munich, Munich, Germany.
[3] CSSB Centre for Structural Systems Biology, Deutsches Elektronen-Synchrotron DESY, Hamburg, Germany.

https://doi.org/10.1016/j.bios.2026.118682
Received 19 December 2025; Received in revised form 23 March 2026; Accepted 30 March 2026
Available online 12 April 2026

triggers in biosensors, or replace inorganic components in electronic devices with bioorganic counterparts (Rivnay et al., 2017).

However, interfacing biology with electronics is not straightforward, as communication within biological systems often cannot be directly connected to traditional electronic infrastructures (Liu, 2021; Chenani et al., 2024). Exoelectrogenic microorganisms represent a notable exception, which can thrive under anoxic conditions by oxidizing organic or inorganic compounds and connecting this process to a respiratory electron transfer chain that typically terminates at outer membrane proteins on the cell surface. These outer membrane proteins are multiheme *c*-type cytochromes that function similarly to wires, transferring electrons along their three-dimensional structure (Reguera et al., 2005; White et al., 2013). The structures of several of these cytochromes have been extensively studied, and the electron transfer pathways from heme center to heme center are largely understood (Paquete et al., 2022). Genetic engineering of these exoelectrogenic microorganisms has enabled the development of biosensors, where promoters for specific components of the electron transfer chain were linked to sensor domains for different analytes (Golitsch et al., 2013; Webster et al., 2014; Si et al., 2015). Among exoelectrogenic model organisms, *Shewanella oneidensis* is one of the best-characterized, alongside *Geobacter sulfurreducens*. Although *S. oneidensis* typically achieves lower current densities in bioelectrochemical systems than *G. sulfurreducens*, its amenability to genetic manipulation and facultatively anaerobic lifestyle make it a particularly versatile chassis for bioelectronic applications and the organism of choice in the present study.

Despite these advancements, leveraging whole-cell biocatalysts still presents challenges in establishing an effective interface between biology and electronics. The attachment of microorganisms to inorganic electrodes plays a pivotal role (Catania et al., 2021). Many sustainable conductive materials exhibit disadvantages due to their generally hydrophobic properties, which limit the robust and rapid attachment of microorganisms. After initial attachment, the microorganisms typically begin to produce extracellular polymeric substances (EPS) composed mainly of sugar polymers, DNA, and proteins (Flemming and Wingender, 2010; Flemming et al., 2023). While some organisms can generate a conductive extracellular matrix aided by protein nanowires, this capability is not widely distributed. Consequently, EPS formation can act as an insulator that shields electron transfer (Xiao et al., 2017). To advance the biology-electronics interface, several studies have reported the use of polymers to connect the organisms with a conductive matrix to the electrode, thereby increasing current output (Zajdel et al., 2018; McCuskey et al., 2020; Knoll et al., 2022). In these cases, the polymer serves not only as a connector between cells and electronics but also enhances the electrode structure by increasing its surface area. For example, Zajdel and colleagues (2018) embedded *S. oneidensis* in a printable conductive PEDOT:PSS matrix, resulting in a 20-fold increase in current output, while Knoll et al. (2022) produced a synthetic hydrogel composed of *S. oneidensis* and conductive agarose, which was sprayed onto electrodes and increased current output ninefold (1324 mA m^{-2}). Similarly, McCuskey et al. (2020) created a biocomposite of *S. oneidensis* mixed with a polyelectrolyte, leading to a 150-fold increase in current output when deposited on a gold electrode. However, a significant challenge that remains unresolved is how to establish a direct conductive interface between biological cells and stable electrodes without using the polyelectrolytes mentioned above. In this study, we have developed a pathway toward this goal using the SpyTag/SpyCatcher technology and the outer membrane cytochrome MtrC from *S. oneidensis*. The SpyTag/SpyCatcher technology is based on the CnaB2 protein domain from *Streptococcus pyogenes* (Spy), which can be divided into a 13-amino-acid-long polypeptide (SpyTag) and a 116-amino-acid-long polypeptide (SpyCatcher). When these two components come into contact under diverse conditions, they spontaneously form an isopeptide bond (Zakeri et al., 2012).

Toward this, we developed a transposon screen to integrate the sequence for a SpyTag polypeptide at arbitrary positions within the *mtrC* gene and screened for *S. oneidensis* cells expressing the MtrC-SpyTag versions, which retained MtrC functionality and displayed a surface exposed SpyTag. We characterized three positions of particular interest due to their location within the MtrC structure and proximity to heme centers, assessing their potential to bind cells to electrodes and form an advanced direct cell-electrode interface. All three MtrC-SpyTag constructs remain functional and display a surface accessible SpyTag enabling covalent coupling of cells to artificial surfaces. Moreover, we could show that this crosslinking system can be used to covalently and conductively couple cells to electrodes and therefore enhance charge transfer in these systems.

2. Methods

2.1. Cell cultivation

E. coli and *S. oneidensis* were grown under oxic conditions in LB-Medium (10 g L^{-1} tryptone, 5 g L^{-1} yeast extract, 5 g L^{-1} NaCl) at 37 °C or 30 °C, respectively.

Anoxic growth of *S. oneidensis* was carried out in M4 minimal medium (2.21 g L^{-1} K_2HPO_4, 0.99 g L^{-1} KH_2PO_4, 87.70 g L^{-1} $NaHCO_3$, 11.89 g L^{-1} $(NH_4)SO_4$) supplemented with 0.1 mM $MgCl_2$, 1 mM $CaSO_4$, 1 g L^{-1} caseine hydrolysate and trace elements (2.50 g L^{-1} $Na_2EDTA \bullet 2 H_2O$, 21.30 mg L^{-1} $MnSO_4 \bullet H_2O$, 58.40 mg L^{-1} NaCl, 107.40 mg L^{-1} $FeCl_2 \bullet 4 H_20$, 119.00 mg L^{-1} $CoCl_2 \bullet 6 H_2O$, 30.00 mg L^{-1} $ZnSO_4 \bullet 7 H_20$, 5.00 mg L^{-1} $CuSO_4 \bullet 5 H_2O$, 351.00 mg L^{-1} H_3BO_3, 93.60 mg L^{-1} $Na_2MoO_4 \bullet 2 H_2O$, 119.00 mg L^{-1} $NiCl_2 \bullet 6 H_2O$, 28.30 mg L^{-1} Na_2SeO_4). Sodium D,L-lactate (5.60 g L^{-1}) served as carbon source and electron donor, ferric citrate (12.25 g L^{-1}) as electron acceptor.

If needed, kanamycin (85,83 μM), tetracycline hydrochloride (31.19 μM) or L-arabinose (100 μM or 5 mM) were added after autoclaving.

2.2. Vector and strain construction

Stains used in this study and the respective genotypes are listed in Table S1. The primers used for amplification and sequencing are shown in Table S2.

2.3. Randomized integration of genetic elements in mtrC

Random transposon mutagenesis and subsequent *spytag* integration were carried out as illustrated in Fig. 1. Briefly, the vector pBAD202 (one μL) was linearized by digestion with NcoI-HF and PmeI (one μL each; New England Biolabs, USA). Primer 1 and 2 were used to amplify *mtrC* with 25 bp overlap to the linearized vector with *S. oneidensis* gDNA as template. A transposon, that confers a tetracycline resistance, was directly and randomized integrated into the purified *mtrC* amplicon using the EZ-Tn5 (TET-1) Insertion Kit according to the manufactures protocol with the exception that amplicon DNA was used instead of plasmid DNA (Biozym Scientific, Germany, **a**). After stopping the reaction, the DNA was purified with AMPure XP beads (Beckman Coulter, USA) to remove the enzymes. The purified, transposed DNA was assembled with the linearized vector using the Gibson Assembly Master® Mix (New England Biolabs, USA) with the linearized vector (**b**). 10 μL of the assembled constructs were transformed via electroporation into NEB 10beta *E. coli* (New England Biolabs, USA) cells and plated on tetracycline selection plates, ensuring that only vectors containing *mtrC* with the transposon inserted were able to grow (**c**). Several thousand colonies were collected, washed off the plate and united in one reaction tube. One μg of the pooled plasmid DNA (isolated using the Wizard Plus Minipreps DNA Purification Kit, Promega, Germany) was then digested with a pair of single-cutting restriction enzymes (KpnI-HF and SbfI-HF; New England Biolabs, USA) to excise the tetracycline resistance cassette and generate uniform ends regardless of transposon integration position

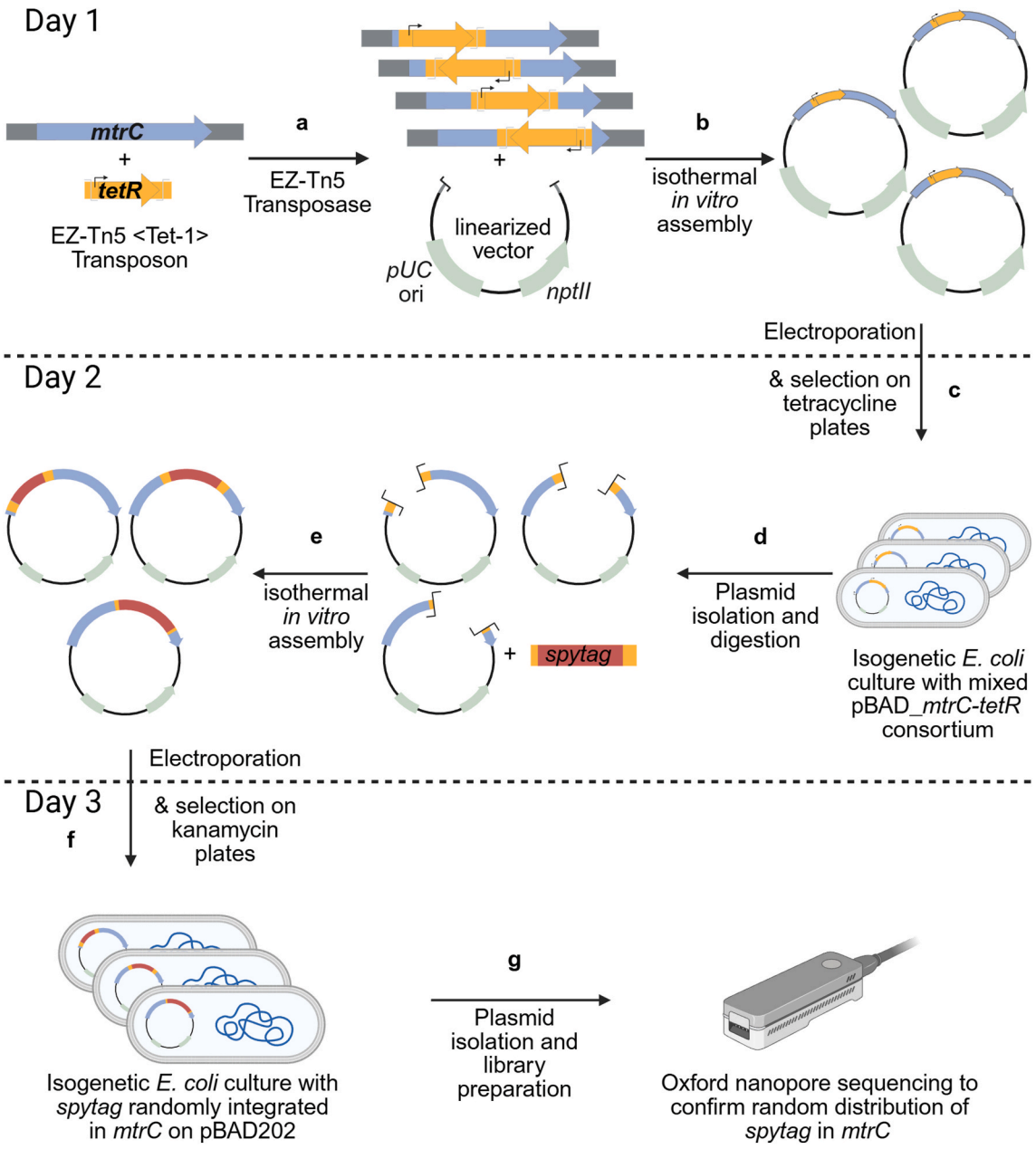

Fig. 1. Cloning workflow for random integration of the *spytag* in *mtrC* on a pBAD plasmid. A detailed description is given in the text.

(d). Primer 3 and 4 were used to amplify the *spytag* with overlapping regions to the linearized plasmid using synthetic DNA (Fig. S1) as a template followed by Gibson assembly (**e**, **f**). The resulting cell suspension was plated on kanamycin plates to ensure plasmid uptake. Several thousand colonies were reunited and nanopore sequencing was employed with the mixed plasmid consortium (**g**). The sequenced mixed plasmid consortium was finally transformed into a *S. oneidensis* Δ*mtrC* strain (Schuetz et al., 2009) via electroporation as described earlier (Corts et al., 2019). Again, several thousand colonies were generated to conduct the screening shown in Fig. 2.

2.4. Plasmid construction

One μg of the pBAD vector was linearized using one μL of each restriction enzyme (NcoI-HF, PmeI, NEB) in CutSmart buffer for 1 h. The inserts for the single integration plasmids were synthesized as a string (Thermo Fisher Scientific, USA) and assembled with the linearized pBAD using a Gibson assembly Mix (NEB, Germany) according to the manufacturers protocol. The plasmids were first transformed into an *E. coli* DH5alphaZI strain (Lutz and Hermann, 1997), sequence verified via Sanger sequencing, and then introduced into the *S. oneidensis* ΔOMC strain via electroporation following the protocol reported by Corts et al. (2019). The synthesized sequences for the *spytag* (Fig. S1), *mtrC-spytag314* (Fig. S2), *mtrC-spytag417* (Fig. S3) and *mtrC-spytag603* (Fig. S4) are given in the supplemental information.

2.5. SpyCatcher functionalization of maleimide beads

SpyCatcher3-CYS (TZC025CYS) was purchased from Bio-Rad Laboratories (USA) and covalently coupled to Maleimide Mono Mag Magnetic Beads (4.5 μm, RayBiotech, USA). Therefore, SpyCatcher3-CYS was incubated for 1 h with 5 mM Dithiothreitol (DTT) to reduce dimers, followed by size exclusion chromatography using the Micro Bio-Spin™ P-6 Gel Columns (Bio-Rad Laboratories, USA) to remove excess

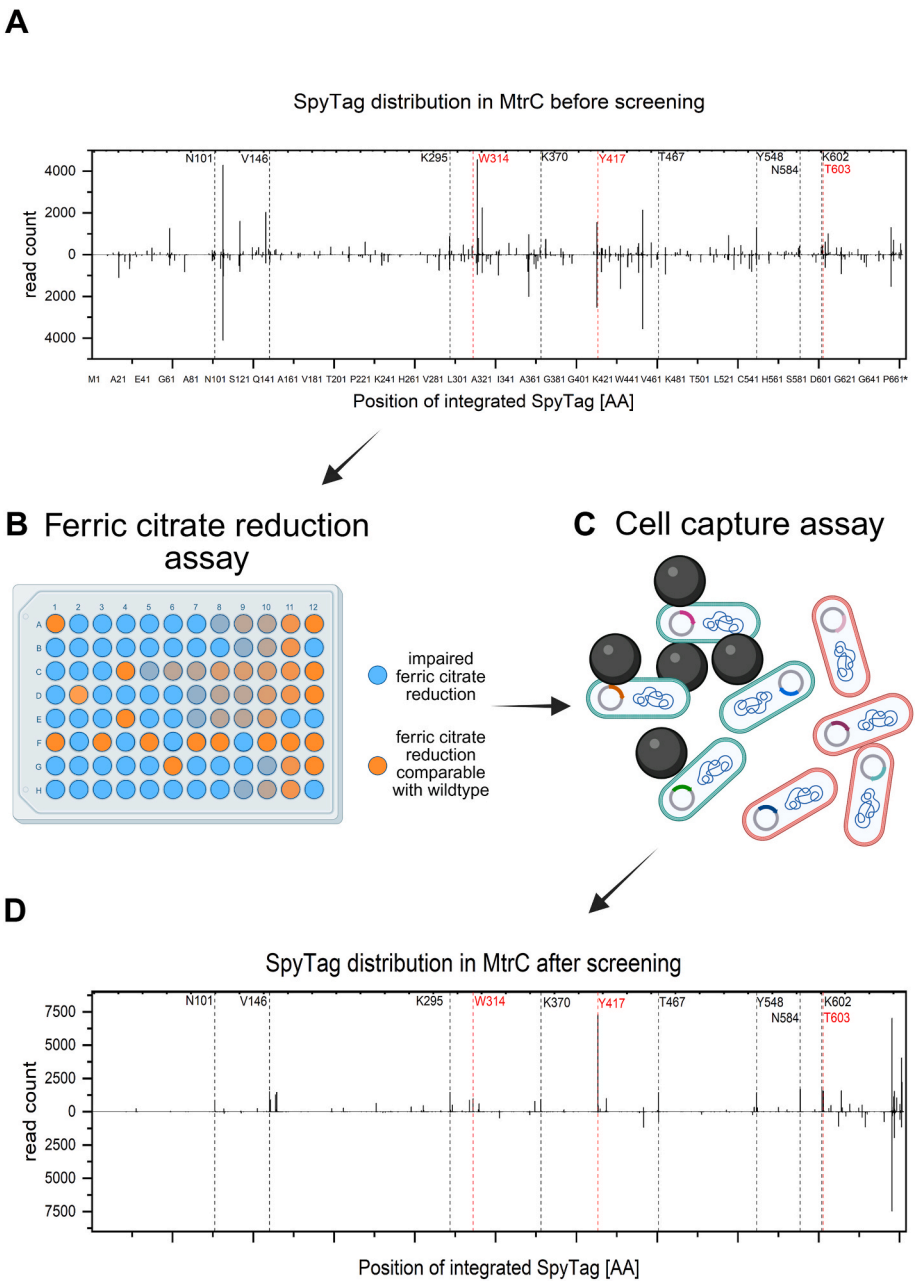

Fig. 2. Initial screen to identify suitable SpyTag integrations in MtrC expressed in a *S. oneidensis* Δ*mtrC* strain. **A)** Oxford nanopore sequencing results of a mixed pBAD_*mtrC-spytag* plasmid consortium isolated from *E. coli* cells. The x-axis represents an integration at the respective nucleotide of *mtrC*, while the y-axis shows the abundance of the reads with an integration in the reading direction pointing upwards and an integration against reading direction pointing downwards. This plasmid consortium represents the library that was introduced in a *S. oneidensis* Δ*mtrC* strain. **B)** 1920 single *S. oneidensis* pBAD_*mtrC-spytag*$_{mix}$ colonies were picked and patched in individual wells of 96-well plates containing anoxic minimal medium with 50 mM ferric citrate as the sole electron acceptor and 50 mM lactate as carbon source. Hence, each well contains cells with a distinct *spytag* integration in *mtrC*. Cells from wells showing the fastest ferric citrate reduction (top 15%) were reunited and incubated together with magnetic beads displaying the SpyCatcher in order to bind the cells with an exposed SpyTag to the beads. **C)** A magnetic rack was used to pull down the cell-bead suspension and remove unbound cells in the supernatant. The cell-bead suspension was rinsed with PBS while keeping it on the magnet to remove the remaining unbound cells. Subsequently, the cell-bead suspension was re-grown in LB medium containing 85.83 μM kanamycin, the plasmids were isolated and re-sequenced. **D)** The results of the sequencing represent the plasmid consortium after the two screening steps that have been carried out. Grey and red lines highlight the most abundant positions, while the red lines also highlight the mutants that were used in further experiments. As expected, mainly integrations in reading direction and in-frame endured the screening procedure. (For interpretation of the references to colour in this figure legend, the reader is referred to the Web version of this article.)

reducing agents. SpyCatcher3-CYS monomers were coupled to the beads directly after reducing the dimers, following the manufacturers protocol. Additionally, the functionalized beads were incubated with 0.7 mg mL^{-1} cysteine for 2 h to saturate free maleimide groups. Functionalized beads were freshly made for each experiment, and purified SpyTag-GFP was used to qualitatively examine successful coupling using fluorescence microscopy.

2.6. Initial screen of mixed plasmid consortium

Single *S. oneidensis* Δ*mtrC* MtrC-SpyTag$_{mix}$ colonies were grown in 96-well plates with oxic LB Medium supplemented with kanamycin and

transferred to anoxic ferric citrate medium with 100 μM arabinose and 85,83 μM kanamycin using a sterile 96-pin microplate replicator (CR1000, EnzyScreen, Netherlands). Ferric citrate reduction correlates with an absorption peak at 390 nm which was used to discriminate between iron reducing and non-iron reducing colonies. Iron reducing cells were reunited, adjusted to an OD_{600} of 0.2 and incubated together with SpyCatcher functionalized magnetic beads for 1 h. The magnetic bead cell suspension was washed three times in phosphate buffered saline (PBS; 136.9 mM NaCl, 2.7 mM KCl, 10.1 mM $NaPO_4$, 1.8 mM KPO_4 adjusted to pH 7.4 with HCl) on a magnetic rack, and the remaining cell bead suspension was used to inoculate LB medium with kanamycin. Plasmids were isolated (Wizard Plus Minipreps DNA Purification Kit, Promega, Germany) after the cultures had reached the stationary phase.

2.7. Oxford nanopore sequencing

Plasmid isolation for nanopore sequencing was carried out using the Wizard Plus Minipreps DNA Purification Kit (Promega, Germany). One μg of plasmid DNA isolated from the consortium was linearized using one μL NdeI-HF (New England Biolabs, UK) prior to library preparation. The library of the mixed plasmid consortium for nanopore sequencing was prepared using the native barcoding kit 24 V14 and sequenced on a MinION device with an R10.4.1 flowcell (Oxford Nanopore Technologies, UK). All procedures were performed according to the manufacturer's instructions. Basecalling was performed using Guppy v.3.5.2 in superaccuracy mode, which included read filtering for quality and trimming of adapters and barcodes.

A database of theoretical possible plasmids was constructed with a Python script of all possible versions of transposon sequences/spy-tag sequences and used as a target for blastn of sequencing reads in the target gene (word size 20, min e-value 10^{-5}). Hits matching the inserted sequence with bordering sequences were selected and counted for each possible construct.

2.8. Fluorescence microscopy of S. oneidensis cells to SpyCatcher functionalized magnetic beads

Induced cells were incubated with anoxic ferric citrate medium at 30 °C overnight. Afterwards cells were stained with 5 μM green fluorescent dye Syto9 (Thermo Fisher Scientific, USA) for 30 min. Excess Syto9 was removed through washing three times with PBS by centrifugation (16,000 g, 1 min). Stained cells were incubated together with SpyCatcher functionalized magnetic beads for 1 h and thereafter washed three times with PBS on a magnetic rack. Microscopy was carried out using the DM5500 B (Leica Microsystems, Germany) with a HCX PL Fluotar objective with Y3 and L5 filter, respectively. Images were processed with Fiji (Schindelin et al., 2012).

2.9. Growth curve

20% (v/v) of an overnight LB culture was transferred into fresh LB medium and induced with 5 mM arabinose for 6 h. The cells were again transferred into fresh medium supplemented with 5 mM arabinose and grown overnight. This culture was washed three times in M4 salts and introduced into an anoxic tent. Triplicates were inoculated to an OD_{600} of 0.04 in 200 μl M4 medium with 85,83 μM kanamycin, 50 mM D,L-lactate as electron donor and carbon source and 50 mM ferric citrate as the sole electron acceptor. Growth was measured in a microplate reader (infinite 200pro, Tecan, Switzerland). The optical pathlength was corrected to 1 cm using the pathlength correction function of the infinite 200pro reader.

2.10. Cell-bead binding assay

Cells were pre-grown in anoxic M4 medium with ferric citrate as the sole electron acceptor and harvested in the exponential phase. 90 μL cell suspension (OD_{600} of 2 in PBS) was mixed with 90 μL magnetic maleimide beads and incubated on a rotary wheel to keep the beads in suspension at room temperature for 6 h. The suspension was then pulled down on a magnetic rack and washed three times with PBS to remove unbound cells. The remaining beads with covalently coupled cells were resuspended in 40 μL PBS, boiled at 98 °C for 10 min to release DNA of the lysed cells. Beads were pelleted again using a magnetic rack and 5 μL of the supernatant was used for quantitative real-time PCR with primers 5 and 6 as described elsewhere (Philipp et al., 2025). Briefly, the gene *mioC*, which is present in all strains, was used to extrapolate the total cell count. A dilution series of *S. oneidensis* cells with a defined cell number served as standard curve.

2.11. Linear sweep voltammetry

For assessing the electrical connection of the different *mtrC*-SpyTag variants onto a metallic surface, linear sweep voltammetry (LSV) was employed. 75 μL gold coated magnetic particle suspension (CD Bioparticles, WHM-GC06) were added to 30 μL reduced SpyCatcher3-CYS and incubated overnight in a thermoshaker (1500 rpm, 4 °C) to functionalize the magnetic beads with SpyCatcher. 10 μg mL^{-1} cysteine (final concentration) was added and incubated for 2 h at room temperature to saturate the gold surface and prevent nonspecific binding of cells. Afterwards, the functionalized beads were washed twice with PBS on a magnetic rack and then incubated with OD_{600} of 1 of cells either containing *mtrC*-SpyTag or a control strain without SpyTag for 4 h at 30 °C on a rotating mixer. The bead-cell-suspensions were washed with 40 μL PBS on a magnetic rack. In the experiment that mimicked washout of redox-mediators in flow-through applications two additional washing steps with 40 μL PBS were carried out.

For LSV assessment, a 4 × 4 mm permanent NdFeB magnet (Supermagnete, Germany) was positioned on the rearside of the working electrode of a screen-printed gold electrode (SPE, Pineresearch, RRPE2001AU). The working electrode had a diameter of 2 mm. The counter electrode was also consisting of gold. The reference electrode was made of Ag/AgCl. LSV was first performed with bare electrodes in 1 mL anoxic PBS and afterwards 10 μL of the corresponding bead-cell suspension was pipetted onto the working electrode and LSV was measured again. LSV was carried out in a range from −0.5 V to 0.5 V (vs. Ag/AgCl) with a scan rate of 100 mV s^{-1} and the headspace was constantly kept anoxic by purging with argon.

The software QSOAS (Fourmond, 2016) was used to process raw data of the linear sweep voltammetry. The commands “baseline” and “filter-fft” were used to subtract the baseline and remove the noise, respectively. The raw data are shown in Fig. S9 and Fig. S10.

2.12. Chronoamperometry

To further assess the direct covalent cell-electrode linkage established by MtrC-SpyTag603 relative to the native MtrC control strain, and to evaluate its potential utility in a biosensing context, a chronoamperometry experiment was performed using the same screen-printed gold electrodes (SPE, Pineresearch, RRPE2001AU) described above. The working electrodes were directly functionalized by applying 5 μL of reduced SpyCatcher3-CYS and incubating for 2 h at room temperature. Cysteine was then added to a final concentration of 10 μg mL^{-1} and incubated overnight at 4 °C to saturate remaining free gold surface sites and minimize nonspecific cell binding. The functionalized SPEs were washed twice with PBS, electrically connected to a potentiostat, and placed in 50 mL vials containing 30 mL of a cell suspension (OD_{600} = 1) in anoxic M4 minimal medium supplemented with 50 mM lactate, using either MtrC-SpyTag603-expressing cells or the native MtrC control. Chronoamperometry was conducted at an applied potential of 0 V vs. Ag/AgCl. After 120 min, the measurement was paused and the medium was exchanged with 30 mL of fresh anoxic M4 minimal medium supplemented with 50 mM lactate to mimic the washout of planktonic

cells and soluble redox mediators in a flow-through system. Current production was then monitored for a further 30 min. Subsequently, a more stringent washing step was applied by repeatedly pipetting PBS directly onto the working electrode surface to approximate hydrodynamic shear stress on electrode-attached cells under flow-through conditions. The SPE was then placed in 30 mL anoxic PBS and current production was monitored for a final 30 min period. All experiments were performed in duplicate, and the headspace of each reactor was maintained anoxic throughout by continuous purging with nitrogen gas.

2.12.1. Cell counting on working electrode surface

Directly after stopping the chronoamperometry experiment the working electrodes were stained with DAPI and fluorescence microscopy of the whole working electrode surface was carried out. For this an ECHO Revolution microscope with U-PLAN PHASE FLUORITE 60× objective (LWD, Ph2) was employed. In order to visualize the whole electrode surface in one image, 25 × 25 singular microscope images were taken and the built in ECHO image stitching function was used. Thereafter, the corresponding image was analyzed via (Fiji Is Just) ImageJ version 2.1.0/1.53 (Schindelin et al., 2012). The 2 mm diameter circular electrode surface area was cropped and an appropriate threshold was set (2846, 36246). The "analyze particles" command was applied for a size of 0.5 to 4.5 μm^2, followed by "count". Threshold and particle size were set in a way to reliably count cells and minimize background.

3. Results

In this study, we set out to use the SpyTag/SpyCatcher system integrated into MtrC to covalently and conductively bind *S. oneidensis* to electrode surfaces. However, the successful implementation of this system depends on two key factors. First, the surface displayed SpyTag should be integrated in an exposed location to facilitate SpyCatcher coupling without steric hindrance. Second, integration of the SpyTag should not disrupt MtrC structure in order to maintain functionality and therefore electron transfer via the MtrCAB electron transport chain. Hence, a transposon screen was developed to identify integration positions matching the mentioned criteria using a high-throughput screen.

3.1. Screening for suitable spytag integration positions in mtrC

A hyperactive Tn5 transposase (Goryshin and Reznikoff, 1998) was used to randomly integrate a tetracycline resistance gene in a *mtrC* amplicon. The mixture of *mtrC-tetR* constructs was cloned onto a plasmid and introduced into *E. coli* cells. Several thousand colonies were collected and the whole plasmid consortium was sequenced. As expected, the transposon was integrated in both directions, in and against the reading direction. Moreover, an integration after almost every nucleotide could be observed without any selection towards integrations in the reading frame of MtrC (Fig. S5). In the next step, the tetracycline resistance was excised using unique restriction enzymes in the transposon sequence. Hence, every single plasmid, regardless of the integration position and direction, had now identical overlaps that could be used to integrate the *spytag* in *mtrC* via isothermal *in vitro* assembly. The detailed cloning workflow is depicted in Fig. 1. The resulting mixed plasmid consortium pBAD_*mtrC-spytag*$_{mix}$ was sequenced, and a similar pattern as for the initial transposon integration could be observed (Fig. 2A). This was expected since a screen for functionality or surface accessibility had not yet been performed. The plasmid consortium was then introduced in *S. oneidensis* Δ*mtrC* strain, which is characterized by severely impaired ferric citrate reduction compared to the wildtype strain (Gao et al., 2010). We inoculated 1920 single colonies in wells of microtiter plates containing a selective medium with ferric citrate as the sole electron acceptor and screened for strains that were able to grow under these conditions (Fig. 2B). The most efficient iron reducing cells were then reunited (280 wells in total), incubated together with SpyCatcher functionalized magnetic beads and pulled down using a magnetic rack (Fig. 2C). The selected cells contain a functional MtrC, as they were able to reduce ferric citrate, and also display a surface exposed SpyTag which is essential for binding to the SpyCatcher functionalized magnetic beads. After conducting both screens subsequently, plasmids were re-sequenced using nanopore sequencing. We refer to this screened culture in the following as MtrC-SpyTag$_{selected}$.

Sequencing of the resulting MtrC-SpyTag$_{selected}$ culture predominantly revealed integrations in the correct reading direction and in-frame, ensuring proper translation of MtrC as well as the SpyTag motif (Fig. 2D). Interestingly, mostly broad integration regions and not distinct integration positions appeared in the sequencing. Of note, at the 3′ end of *mtrC* (downstream of nucleotide 1811), some integrations still appear against the reading direction, which is probably due to a small number of unbound cells remaining after the bead wash steps. Those cells could then propagate faster than the bound cells and would therefore be over-represented in the plasmid sequencing. We excluded those integrations from further analysis since the resulting MtrC-SpyTag constructs could not confer SpyTag binding. Otherwise, the most frequent integrations can be attributed to a growth advantage with ferric citrate as the sole electron acceptor, efficient bead binding or both.

3.2. Fluorescence microscopy of MtrC-SpyTag$_{selected}$ cultures reveals cell-bead agglomerates

To visualize the cell-bead binding, *S. oneidensis* Δ*mtrC mtrC-spytag*$_{selected}$ expressing cells were stained with a green fluorescent dye (Syto9) and incubated together with the SpyCatcher functionalized magnetic beads, which show a red auto-fluorescence. The same strain with the only difference that native MtrC, instead of MtrC-SpyTag$_{selected}$, was overexpressed, served as a negative control. In this sample, no cell-bead binding should be possible since the SpyTag is missing. The cell-bead suspension was washed three times on a magnetic rack in order to remove unbound cells. These washed suspensions were used for fluorescence microscopy (Fig. 3). Indeed, cell-bead agglomerates were observed only for the MtrC-SpyTag$_{selected}$ culture, while only a few unbound cells remained in the negative control (Fig. 3, Fig. S6). Although the experiment is only a qualitative indicator for coupling of the magnetic beads to cells expressing the SpyTag its results were corroborated in further analyses (see below).

3.3. Visualization of integration positions in the 3D structure of MtrC and distance to heme groups

To enable more detailed characterization, a selection rationale was developed to identify transposon integration positions either at surface-accessible sites or in close proximity to a heme group. This was intended to position the redox-active moieties near a biosensor surface, thereby facilitating covalent and electrically conductive cell-to-electrode binding. To this end, the distances from the Cα atom of each residue at the respective integration position to all heme groups were measured (Table 1), providing a basis for identifying the most promising positions for conductive crosslinking.

In order to be able to conduct experiments with pure cultures, we narrowed the selection down to three integration positions:

- First, the most abundant integration position (MtrC-SpyTag417), located in domain III of MtrC, which is most likely well suited for covalent cell coupling.
- Second, a position with average abundance and a fairly exposed location (MtrC-SpyTag603), located in domain IV of MtrC.
- Third an integration which is interestingly in very close proximity to several heme groups (MtrC-SpyTag314) and integrated in the flexible hinge region of MtrC (domain II).

Subsequently, the AlphaFold 3 server (Abramson et al., 2024) was

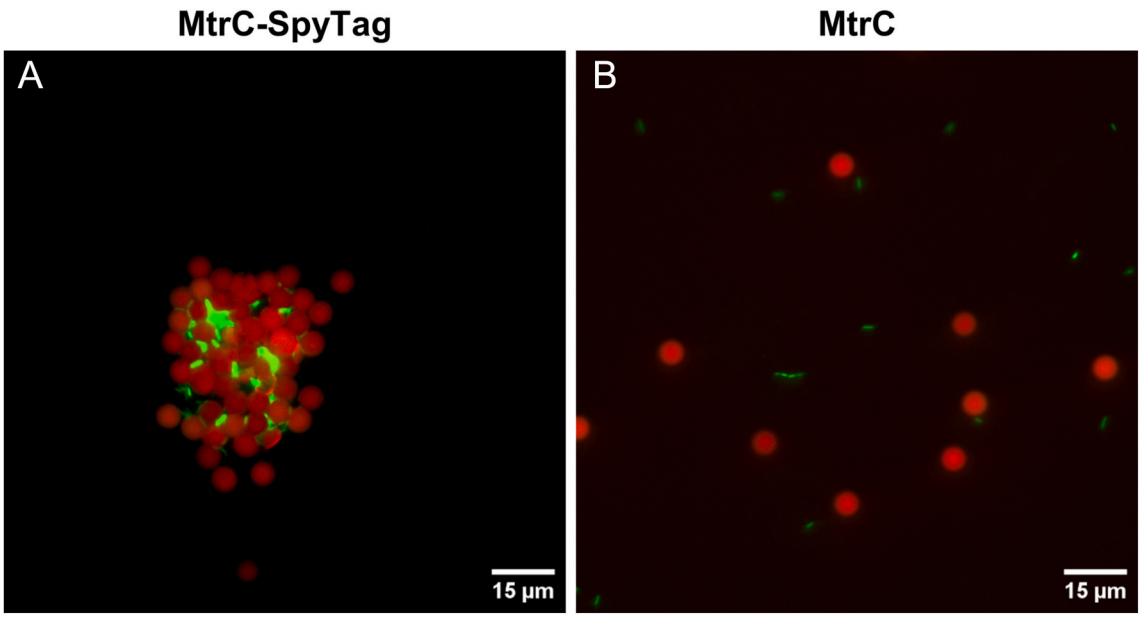

Fig. 3. Fluorescence microscopy of Syto9 stained cells (green) bound to SpyCatcher functionalized magnetic beads (red). The cells were incubated together with the beads displaying a SpyCatcher and the cell-bead suspension was washed on a magnetic rack to remove unbound cells. **A)** *S. oneidensis* Δ*mtrC* pBAD_*mtrC-spytag*$_{selected}$. **B)** *S. oneidensis* Δ*mtrC* pBAD_*mtrC*. Agglomerates appeared only in the samples with cells expressing MtrC-SpyTag. In the negative control, a few cells remain after washing the cell bead suspension, but no agglomerates could be observed. (For interpretation of the references to colour in this figure legend, the reader is referred to the Web version of this article.)

Table 1
Minimum distance of the C_α atom of the most abundant integration positions of the SpyTag in MtrC to all heme groups. Shown in bold is the minimal distance of the respective amino acid to a heme group. Highlighted in red are the closest 10 % of all integration positions to a heme group.

Position	1	2	3	4	5	6	7	8	9	10
N101	25.29	22.45	15.20	17.81	**15.18**	37.80	47.55	46.78	49.22	58.37
V146	21.16	**15.42**	24.43	34.55	39.84	31.66	42.84	32.72	30.86	37.63
K295	30.50	30.83	24.00	16.46	**11.48**	38.85	45.12	50.15	52.84	61.99
W314	25.48	31.73	15.60	**10.55**	11.45	31.56	38.01	42.23	48.22	57.53
K370	37.30	49.58	36.86	31.84	37.93	29.59	**25.13**	37.75	46.81	53.84
Y417	44.58	57.52	48.38	46.36	54.29	32.07	**22.72**	34.23	43.35	47.42
T467	26.74	39.17	27.30	23.66	31.39	19.69	**18.08**	29.14	37.75	45.55
Y548	33.54	44.29	41.66	40.88	49.83	20.62	**10.57**	21.83	26.80	30.72
N584	29.98	39.31	38.92	44.36	53.86	20.37	21.40	**9.74**	15.65	18.13
K602	40.21	48.93	49.60	49.25	57.99	28.67	**20.88**	27.27	28.41	29.61
T603	41.38	50.45	50.91	51.01	59.97	29.21	**20.96**	26.52	28.00	28.43

used to predict the structure of the MtrABC-SpyTag constructs and therefore model the surface accessibility of the integrated SpyTags as well as the effect on the protein structure of MtrC. Alignment of the predicted structures to the crystal structure of MtrC from *S. oneidensis* (PDB: 4LM8) and to the MtrCAB complex isolated from *S. baltica* (PDB: 6R2Q) suggests that the SpyTag integration would not affect the MtrC structure (Fig. 4). The model confidence and root mean square deviations are given in Table S3. MtrC-SpyTag417 and MtrC-SpyTag603 have an exposed SpyTag while the MtrC-SpyTag314 is predicted to be located very close to the MtrAB complex and therefore the outer membrane which could result in steric hindrances. In contrast, the flexibility of the hinge region could overcome these steric hindrances and enable binding to a SpyCatcher. The overall confidence of the model is high (Table S3, Figure S8) which suggests that the 3D structure of MtrC is very likely not disturbed. However, the low confidence in the transposon and SpyTag region does not allow to carry out deeper analysis with regards to SpyTag-SpyCatcher binding. To verify functionality, individual plasmids encoding *mtrC* with a SpyTag integrated at each of the three positions (W314, Y417, or T603) were cloned and introduced into an *S. oneidensis* ΔOMC strain lacking all outer-membrane cytochromes (Bücking et al., 2010), a strain incapable of extracellular electron transfer.

3.4. MtrC remains functional for all three integration positions

In order to quantitatively assess the functionality of the MtrC-SpyTag versions, the *S. oneidensis* ΔOMC MtrC-SpyTag pure cultures were tested in a growth experiment with ferric citrate as the sole electron acceptor. Due to the lack of outer-membrane cytochromes, *S. oneidensis* ΔOMC is not able to reduce ferric citrate (Bücking et al., 2010). Similarly, the negative control, *S. oneidensis* ΔOMC carrying an empty plasmid, also did not grow over the time course of the experiment. The growth of the

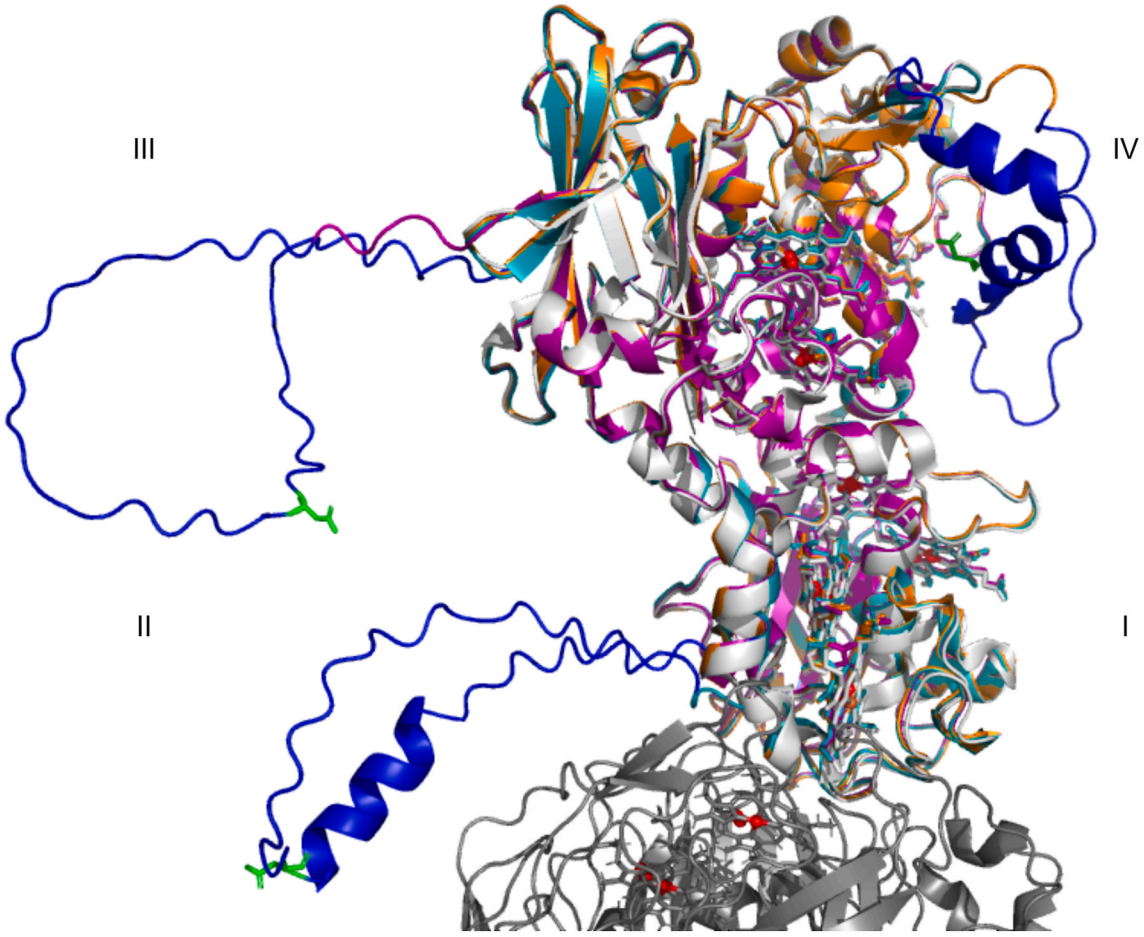

Fig. 4. AlphaFold 3 structural models of MtrC-SpyTag constructs aligned to the MtrCAB complex. MtrAB (dark grey) is derived from the crystal structure of the MtrCAB complex from *S. baltica* (PDB: 6R2Q). AlphaFold 3-predicted structures of MtrC-SpyTag314 (teal), MtrC-SpyTag417 (purple), and MtrC-SpyTag603 (orange) are aligned to the wildtype MtrC crystal structure from *S. oneidensis* (PDB: 4LM8, light grey). The inserted amino acid sequence is highlighted in blue, with the reactive aspartic acid residue of the SpyTag — which forms the covalent isopeptide bond with the SpyCatcher — shown as a green stick. Red spheres represent the iron centers of heme groups, and roman numerals denote the respective structural domains of MtrC. The overall high structural agreement between the predicted and experimental MtrC structures suggests that SpyTag integration does not substantially perturb the native fold of MtrC. Model confidence scores and root mean square deviations relative to PDB: 4LM8 are reported in Table S3. Individual structure alignments for each of the three constructs are shown in Fig. S7. (For interpretation of the references to colour in this figure legend, the reader is referred to the Web version of this article.)

positive control, *S. oneidensis* ΔOMC expressing MtrC without a SpyTag, was similar to the growth of the MtrC-

SpyTag417 and MtrC-SpyTag603 strains (Fig. 5A). The MtrC-SpyTag314 strain had a similar lag phase but a lower maximum growth rate in the exponential phase (Fig. 5B). Although the strains expressing the MtrC variants reduced ferric citrate completely and reached similar maximum ODs, their different growth behavior suggests slight activity differences due to the integration positions of the SpyTag. Nevertheless, all strains were able to reduce ferric citrate and express a functional MtrC. Thus, our first key objective, integrating the SpyTag in MtrC without compromising the enzyme functionality, was fulfilled for all three integration positions.

3.5. MtrC-SpyTag expressing cells can be crosslinked to SpyCatcher functionalized surfaces

To quantitatively assess the binding efficiency of the three individual MtrC-SpyTag constructs, we employed a cell-bead pulldown assay. Cells of each strain were incubated with SpyCatcher-functionalized magnetic beads under identical conditions, and unbound cells were subsequently removed by repeated washing on a magnetic rack. The number of cells remaining covalently coupled to the beads after washing was quantified by qPCR targeting the chromosomal *mioC* gene as a proxy for cell number. All three MtrC-SpyTag variants bound significantly more cells to the SpyCatcher-functionalized beads compared to the negative control strain expressing wildtype MtrC without a SpyTag (unpaired *t*-test, $p < 0.05$), confirming that binding is specifically mediated by the SpyTag/SpyCatcher interaction rather than by nonspecific cell-bead adhesion. Among the three constructs, MtrC-SpyTag417 showed the highest binding efficiency, followed by MtrC-SpyTag603, while MtrC-SpyTag314 exhibited the weakest binding of the three MtrC-SpyTag strains, consistent with its predicted partially occluded surface accessibility in the AlphaFold structural model (Fig. 4,Fig. 6).

In summary, all selected constructs featured a functional MtrC and a surface exposed SpyTag that can be coupled to a SpyCatcher, making them promising candidates for usage in living electronics.

3.6. MtrC-SpyTag accelerates electron transfer to SpyCatcher functionalized electrodes

MtrC-SpyTag417 and MtrC-SpyTag603 were selected to test for potentially altered interaction characteristics to electrode surfaces as both supported faster growth and better SpyCatcher interaction compared to MtrC-SpyTag314. Therefore, magnetic SpyCatcher-goldbeads were used to pull the MtrC-SpyTag cells onto an electrode and current was measured using linear sweep voltammetry. Two peaks,

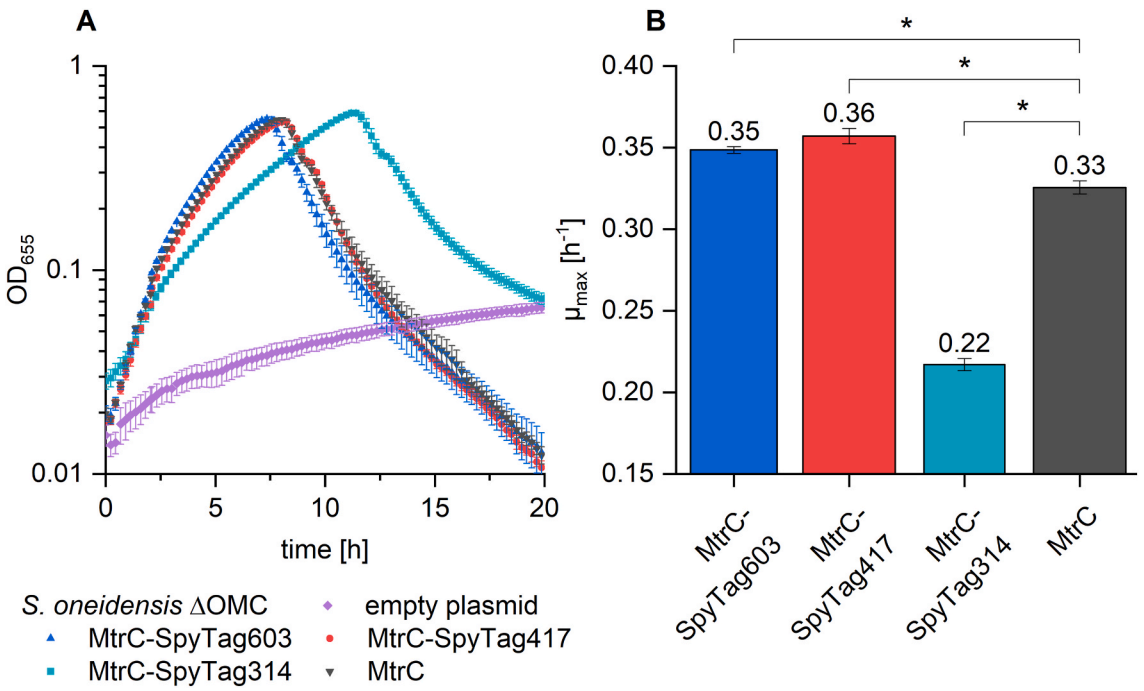

Fig. 5. Growth of *S. oneidensis* ΔOMC strains expressing either MtrC or MtrC-SpyTag variants in anoxic minimal medium with ferric citrate as the sole electron acceptor. The negative control carries only an empty plasmid. **A)** Optical density at 655 nm over the course of time. **B)** Maximum specific growth rate μ_{max} of all strains that reached the exponential phase. Error bars represent standard deviations from three independent replicates (n = 3). All growth rates are significantly different to the wildtype MtrC (unpaired *t*-test, $p < 0.01$).

which can be attributed to cytochrome based-reduction of the electrode, were observed. This finding is in good accordance with the literature identifying redox shuttle, or mediated, electron transfer with an onset potential around −0.2 and −0.1 V vs SHE and direct electron transfer with an onset potential between 0.15 and 0.2 V vs SHE (Carmona-Martinez et al., 2011; Okamoto et al., 2013; Roy et al., 2013, 2014; Xu et al., 2016). However, in our setting, the peaks of the strain expressing wildtype MtrC slightly shifted to higher potentials for mediated as well as direct electron transfer which could be due to different buffer compositions, slightly different pH, or faster sweep rates. Strains expressing MtrC and MtrC-SpyTag versions show identical onset potentials for mediated electron transfer while the peaks are higher and the reduction window is broader for MtrC-SpyTag cells. However, the introduction of a SpyTag into MtrC leads to lower onset potentials for direct electron transfer compared to native MtrC. Again, MtrC-SpyTag redox window as well as peaks are broader and higher, respectively (Fig. 7A).

Integration of the peak areas revealed that the area is over 6-fold (SpyTag603) or > 2-fold (SpyTag417) increased, respectively, compared to the MtrC wild-type expressing strain (Fig. 7B). This increase in charge transfer of the two variants compared to the wild-type is likely due to the expected higher number of cells on the electrode due to binding to the Spy-Catcher beads. The overall charge transfer seems to be highest for MtrC-SpyTag603, the ratio between direct and mediated electron transfer is most favored toward direct electron transfer for this strain accordingly.

To simulate conditions more relevant to flow-through biosensing applications, where soluble redox mediators such as flavins are subject to continuous washout, a second set of LSV measurements was performed after more extensive washing of the cell-bead suspension. Specifically, following the initial gentle wash, two additional washing steps with PBS on a magnetic rack were carried out prior to electrode deposition, thereby progressively depleting the suspension of potential mediators. Under these conditions, the mediated electron transfer peak was abolished, and only the direct electron transfer peak remained detectable (Fig. 7C). This corroborates that the first peak observed under gentle washing conditions (Fig. 7A) is potentially attributable to flavin-mediated electron transfer, while the second peak reflects direct electron transfer via the MtrCAB complex. Both MtrC-SpyTag variants retained a measurable direct electron transfer signal after extensive washing, while the signal of native MtrC was markedly diminished, underscoring the benefit of covalent cell-electrode anchoring for maintaining electrode-relevant electron transfer under washout conditions. Notably, MtrC-SpyTag603 outperformed MtrC-SpyTag417, retaining the strongest direct electron transfer signal of the three strains tested. Quantification of the area under the direct electron transfer peak confirmed that MtrC-SpyTag603 transferred significantly more charge than the native MtrC control (unpaired *t*-test, $p < 0.01$), while the difference between MtrC-SpyTag417 and native MtrC, though consistently in the same direction, did not reach statistical significance under these more stringent conditions (Fig. 7D). Taken together, these results demonstrate that SpyTag integration enhances direct electron transfer robustness under flow-through-relevant conditions, with MtrC-SpyTag603 emerging as the most promising candidate for stable cell-electrode interactions.

3.7. *MtrC-SpyTag generates more robust anodic biofilms in biosensing applications*

Building on the LSV results, MtrC-SpyTag603 was selected for further assessment of its potential applicability in biosensing contexts, given its consistently superior performance in all preceding experiments. As a proof-of-concept, the working electrode of a screen-printed gold electrode was directly functionalized with SpyCatcher and placed in a small-scale microbial electrolysis cell containing either MtrC-SpyTag603 cells or the native MtrC control strain. While screen-printed electrodes represent a simplified model system, they allow controlled assessment of cell-electrode interactions and current production under defined conditions. In a chronoamperometry experiment, the current output of each planktonic cell suspension was first monitored for 120 min under identical conditions. During this initial phase, both strains produced

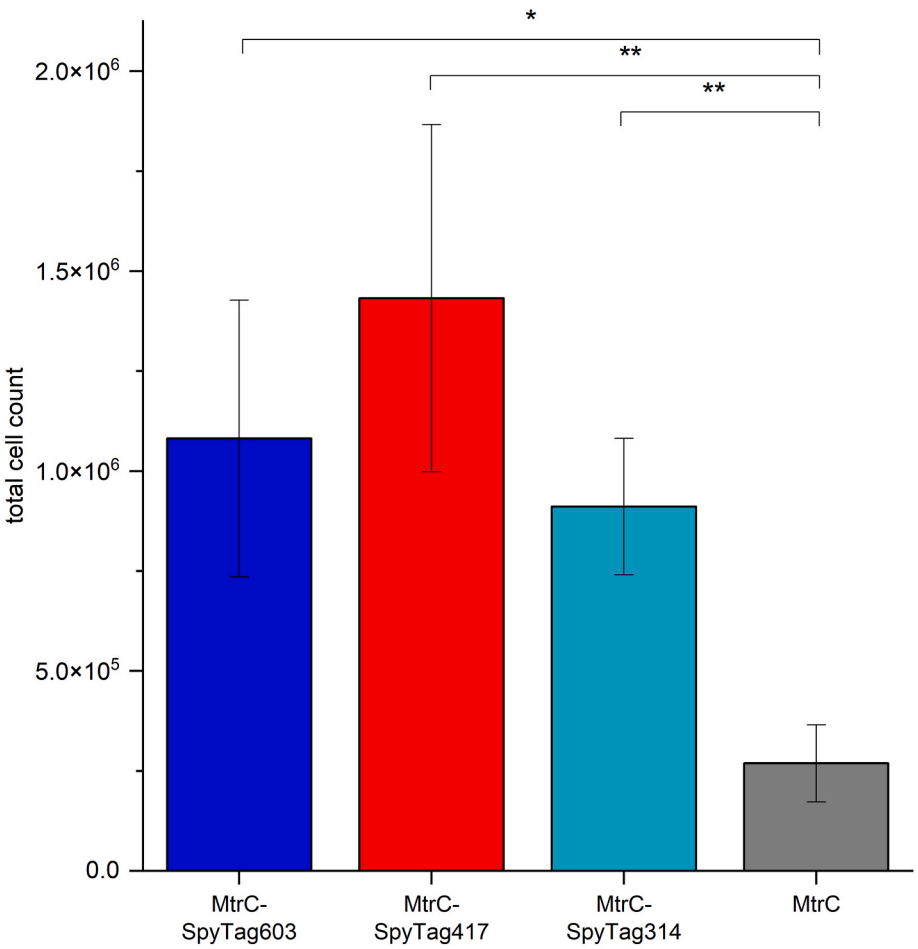

Fig. 6. Number of *S. oneidensis* ΔOMC cells coupled to SpyCatcher-functionalized magnet beads after washing the cell-bead suspension on a magnet. The cell number was quantified using qPCR with *mioC* as the target and cell numbers were calculated using a standard curve with a defined cell number of *S. oneidensis* cells. In all samples with MtrC-SpyTag variants remained significantly more cells in the suspension than in the negative control with cells expressing only MtrC (unpaired *t*-test, *$p < 0.05$, **$p < 0.01$, $n = 3$).

comparable current, with the control reaching a mean steady-state current density of approximately 1 μA cm^{-2} and MtrC-SpyTag603 performing slightly, though not significantly, lower at around 0.6 μA cm^{-2} (Fig. 8A). This comparable initial performance is consistent with the expectation that planktonic electron transfer, which relies primarily on diffusible redox mediators, is not substantially affected by SpyTag integration.

After 120 min, the chronoamperometry was paused and the medium was exchanged with fresh, mediator-free medium to mimic the washout of planktonic cells and soluble redox shuttles in a flow-through setup. Current density was then monitored for a further 30 min. Under these conditions, a clear divergence between the two strains emerged: MtrC-SpyTag603 maintained a stable steady-state current density of approximately 10 nA cm^{-2}, while no positive current could be detected for the native MtrC control (Fig. 8, B). This demonstrates that, at least under the conditions tested here, only cells covalently anchored to the electrode via the SpyTag–SpyCatcher interaction were capable of sustaining electron transfer after mediator washout.

To further assess the robustness of the cell-electrode interface, the measurement was paused a second time and a more stringent washing procedure was applied, in which PBS was repeatedly pipetted directly onto the working electrode surface to approximate hydrodynamic shear stress on electrode-attached cells. It should be noted that the shear forces applied in this way may not fully recapitulate those encountered in real flow-through devices; nonetheless, this step provides a useful qualitative indicator of cell-electrode attachment stability. Following this procedure, current density was monitored for an additional 30 min. MtrC-SpyTag603 still maintained a stable steady-state current density of approximately 5 nA cm^{-2}, while the control continued to produce no detectable positive current (Fig. 8, C). These results suggest that the covalent SpyTag–SpyCatcher linkage confers sufficient mechanical stability to resist cell detachment and sustain direct electron transfer under conditions that disrupt non-specifically attached cells.

To corroborate the electrochemical findings, cell numbers on the working electrode surfaces were quantified by fluorescence microscopy immediately after the conclusion of the chronoamperometry experiment. The empty electrode yielded approximately 400 counts, representing background fluorescence noise. The native MtrC control strain produced a similarly low count of 386 cells, confirming that essentially no cells remained attached to the electrode surface after the washing steps, in full agreement with the absence of detectable current production (Fig. 8D). In contrast, the MtrC-SpyTag603 strain yielded a count of 2467 cells on the electrode surface, directly demonstrating that covalent SpyTag–SpyCatcher coupling effectively retains cells on the electrode even under these more stringent washing conditions (Fig. 8E). Taken together, these proof-of-concept results indicate that SpyTag-mediated covalent cell anchoring can meaningfully improve electrode attachment and direct electron transfer stability, and motivate future assessment of this approach in more complex flow-through device configurations.

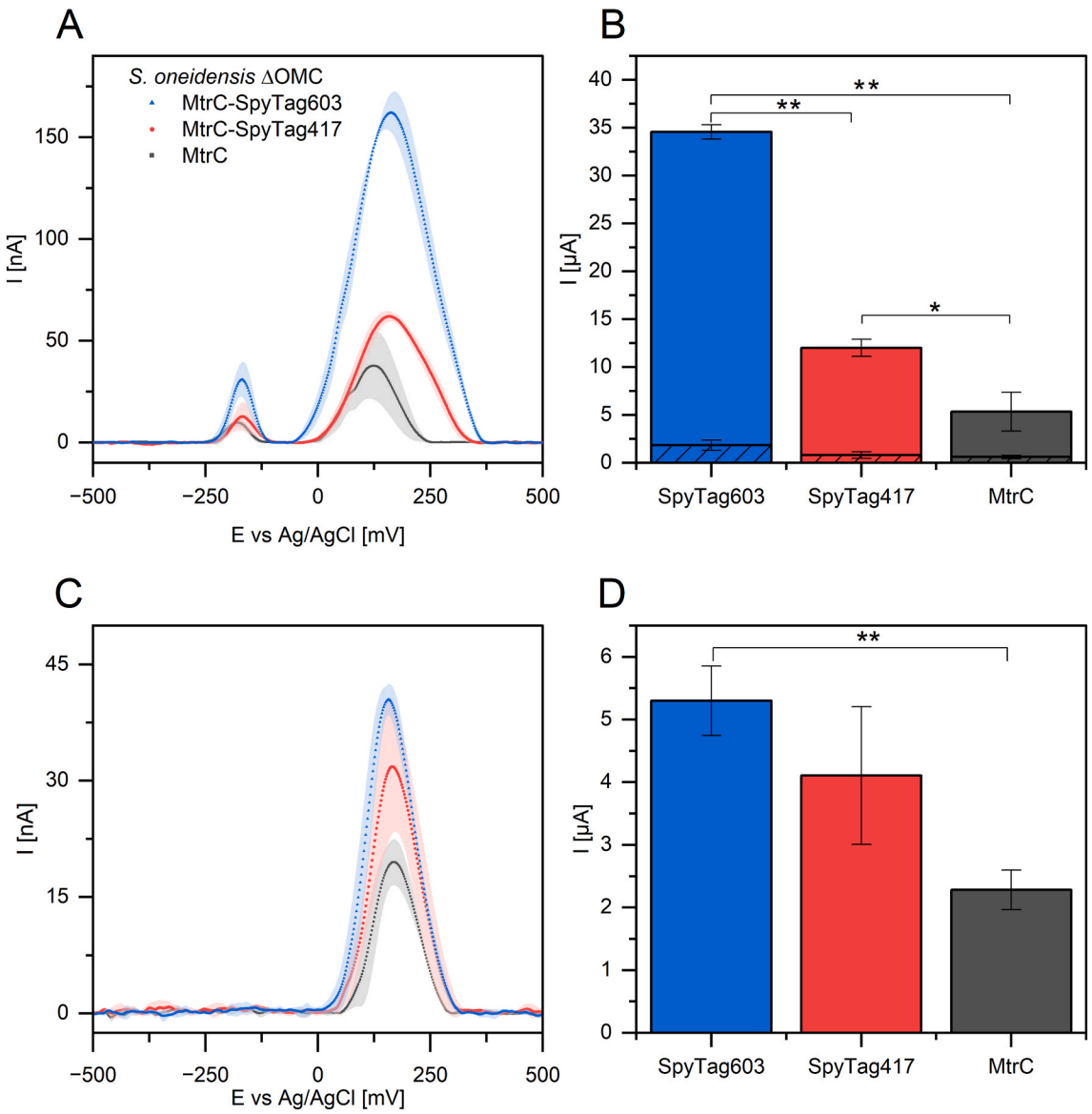

Fig. 7. Linear sweep voltammetry of *S. oneidensis* ΔOMC strains expressing MtrC-SpyTag603 (blue), MtrC-SpyTag417 (red), or native MtrC (grey), coupled to SpyCatcher-functionalized magnetic gold beads and depleted of unbound cells by washing. The washed cell-bead suspensions were deposited onto a screen-printed gold electrode using a permanent magnet and submerged in anoxic PBS. (A) LSV recorded after gentle washing, revealing two distinct current peaks attributable to flavin-mediated electron transfer (onset ~−170 mV vs. Ag/AgCl) and direct electron transfer (onset ~160 mV vs. Ag/AgCl), respectively. (B) Integrated charge transfer for mediated (hatched) and direct (solid) electron transfer peaks from (A). MtrC-SpyTag strains show significantly higher total charge transfer than native MtrC, with the largest share occurring via direct electron transfer. (C) LSV recorded after extensive washing to remove potentially remaining redox mediators. Under these conditions, only the direct electron transfer peak is detectable, corroborating the mediator-independent nature of this signal. (D) Integrated charge transfer for the direct electron transfer peak from (C). MtrC-SpyTag603 shows significantly higher direct charge transfer than native MtrC. Error bars represent standard deviations from independent replicates (n = 3); significance was assessed by unpaired *t*-test (*p < 0.05, **p < 0.01). (For interpretation of the references to colour in this figure legend, the reader is referred to the Web version of this article.)

4. Discussion

In this study, we set up a direct cell-electrode connection which can be applied to bioelectronics. We first established a cloning technique that can be used to integrate any given DNA sequence into arbitrary positions of the gene of interest within a week. To investigate the effect of crosslinker integrations in MtrC, we conducted a high-throughput assay that allows the screening of surface-accessible cell crosslinkers that confer the ability to bind cells to electronics while maintaining the normal function of the key enzyme. Using the screening approach described here, we identified several regions that are potentially suitable for integrating peptides into MtrC and to crosslink cells with SpyCatcher-displaying materials. In a previous study, Lockwood et al. (2024) demonstrated that A293, E344 and A430 can be substituted with non-canonical amino acids (ncAAs) without compromising the structure or functionality of MtrC *in vitro*. However, *in vivo* experiments with FMN as electron acceptor were not carried out with ncAAs incorporated at position A293 due to the location at the interface with the MtrAB complex. Interestingly, this region also appeared in the initial screen conducted in this study (Table 1; N101 and K295), suggesting that it is indeed suitable for the integration of artificial sequences without affecting the functionality of MtrC *in vivo*.

Integration position W314 was of particular interest to us, since it is localized within a flexible hinge region in close proximity to a heme group and was therefore characterized in more detail. The ferric citrate reduction assay and the SpyCatcher-bead binding assay revealed that

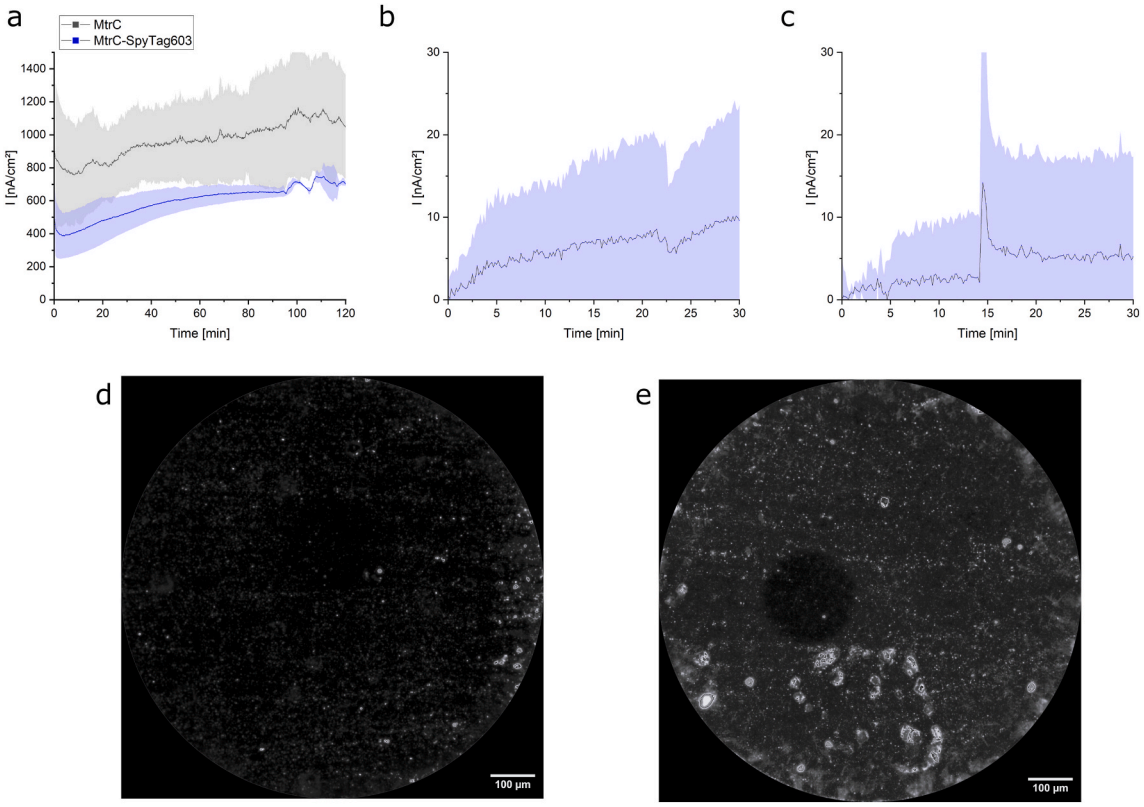

Fig. 8. Assessment of covalent cell-electrode anchoring via MtrC-SpyTag603. The working electrode of a screen-printed gold electrode was directly functionalized with SpyCatcher3-CYS and incubated with either *S. oneidensis* ΔOMC MtrC-SpyTag603 (blue) or the native MtrC control strain (grey) at 0 V vs. Ag/AgCl. (a) Current density during the initial 120 min incubation with planktonic cell suspensions. (b) Current density after medium exchange with fresh lactate-supplemented M4 medium to mimic mediator washout in a flow-through setup. (c) Current density after repeated pipetting of PBS directly onto the electrode surface to approximate hydrodynamic shear stress. Shaded areas represent the range of duplicate measurements. (d, e) Fluorescence microscopy images of DAPI-stained working electrode surfaces after the chronoamperometry experiment for the native MtrC control (d) and MtrC-SpyTag603 (e). Images are stitched composites of 25 × 25 individual fields of view covering the full 2 mm electrode surface. Scale bars = 100 µm. (For interpretation of the references to colour in this figure legend, the reader is referred to the Web version of this article.)

MtrC remains functional and that the SpyTag is accessible, albeit the AlphaFold prediction suggests a sterically hindered orientation towards the MtrAB complex (Fig. 4, Fig. S7 A). This finding highlights that the screen reported here can be used to identify protein regions suitable for synthetic engineering that would have been excluded if using computational biology as the sole decision basis.

However, the other two constructs assessed in this study (MtrC-SpyTag417 and MtrC-SpyTag603) showed even better bead-binding characteristics and higher growth rates with an extracellular electron acceptor. The ferric citrate reduction rates achieved by expression of either MtrC-SpyTag417 or MtrC-SpyTag603 are comparable to those of native MtrC, indicating that there are no negative effects due to the SpyTag integration. This is in good agreement with the study conducted by Lockwood et al. (2024), that showed that E344 and A430, which are in very close proximity to Y417, are interchangeable with non-canonical amino acids without loss of MtrC functionality *in vivo*. Both integration positions, Y417 and T603, showed better bead-binding properties compared to the wildtype MtrC and even MtrC-SpyTag314 which is consistent with the predicted surface accessibility (Fig. 4).

Consequently, these two strains were used in an approach to evaluate the applicability for bioelectronic systems (Fig. 7). While the overall charge transfer could be improved by more than 6-fold, the more significant finding is that the majority of the electrons translocated to the electrode occurred through direct electron transfer. This shift is particularly advantageous for flow-through biosensing systems, where redox shuttles are prone to be washed out and depleted (Engel et al., 2019; Klein et al., 2024), consequently leading to signal drifts and long term instabilities. As *S. oneidensis* is a poor biofilm former on anodes and is usually highly reliant on shuttle-mediated transfer, this is even more relevant. To mimic the washout of redox-mediators and biofilm sheer stress, additional LSVs were performed after more thorough washing of the electrodes, which demonstrated that in flow-through setups electrode attachment and direct electron transfer become more important for stable whole-cell biosensing processes. SpyTag603 showed, in line with the previous experiments, the best direct electron transfer rate before and after thorough washing. Building on this finding, an additional chronoamperometry experiment of this strain versus the control was conducted, which resulted in the same trend, namely higher current densities after medium exchange and washing of electrodes and can be attributed to the covalent anchoring of the cells onto the electrode surface, making the biosensor overall more stable and independent of redox-mediators. This behavior is also reflected in the microscopy data retrieved from SpyTag603 and control electrodes.

The Chronoamperometry experiment acts as exemplary use case for a biosensing application and additionally demonstrates that the electrode surface can directly be functionalized with SpyCatcher to generate stable covalent anchoring of SpyTag cells without the need of employing SpyCatcher-functionalized magnetic beads.

The magnetic beads can nonetheless be utilized for working electrode surface enhancement, which results in signal amplification. A previous study with comparable magnetic nanoparticles focused on this enhancement and no substantial cytotoxicity of the nanoparticles for *S. oneidensis* was observed (Wurst et al., 2024). Moreover, in environmental monitoring scenarios where particle recovery is desirable, the

magnetic properties of the nanoparticles would allow for straightforward reuse of bead-cell conjugates via magnetic separation, further reducing material costs, improving process engineering and minimizing environmental particle release.

The SpyTag/SpyCatcher system offers several advantages over existing surface functionalization strategies for bioelectronics. Approaches such as polymer embedding (e.g., PEDOT:PSS or conductive agarose hydrogels) and polyelectrolyte composites, discussed in the introduction, increase current output by improving electrode architecture and surface area, but rely on passive cell entrapment rather than defined covalent cell-electrode coupling. This means that cell positioning and orientation at the electrode surface remain largely uncontrolled, and the interface is susceptible to mechanical disruption under flow conditions. In contrast, the SpyTag/SpyCatcher system forms an irreversible isopeptide bond, providing a chemically defined and mechanically stable linkage between the cell surface protein MtrC and the electrode. Critically, this bond is formed site-specifically at a defined position within MtrC, ensuring that the electron-transferring cytochrome remains correctly oriented relative to the electrode surface. Furthermore, the SpyCatcher toolbox is commercially available with a broad range of surface-compatible linkers, making this approach readily adaptable to diverse electrode materials and device geometries without requiring custom synthesis of conductive polymers or biocomposites.

Furthermore, the SpyTag-SpyCatcher system is well established and is commercially available with a wide range of attached linkers and can therefore be utilized to functionalize a broad spectrum of already existing bioelectronic sensors (Cai et al., 2025).

Recently, Philipp et al. (2025) demonstrated that MtrC is surface-displayed in *E. coli* strains that express the *S. oneidensis* type II secretion system. This finding suggests that *E. coli*, in conjunction with MtrC-SpyTag, can be utilized as living sensors, thereby expanding the range of substrates that can be detected. To extend the applicability of this approach even further, SpyTag can be exchanged with a SpyCatcher to enable cell-cell crosslinking and, therefore, used to form thick and conductive biofilms. This and even more elaborated MtrC-SpyTag/MtrC-SpyCatcher networks will clearly be the scope of future research.

While the SpyTag/SpyCatcher system effectively addresses the challenge of establishing a stable and direct cell-electrode interface, several other bottlenecks inherent to whole-cell bioelectronic systems remain to be resolved.

The current system relies on plasmid-based expression of the MtrC-SpyTag constructs induced by arabinose, which introduces a degree of genetic and regulatory instability that may be problematic for long-term device operation. Chromosomal integration of the construct would be a necessary step toward a genetically stable production strain suitable for real-world applications.

The obligate requirement for anoxic conditions to sustain extracellular electron transfer in *S. oneidensis* remains a fundamental constraint that this approach does not overcome, limiting applicability in oxic sensing environments. Here, a strategically developed mass transfer limitation for oxygen by depositing high cell densities on the electrode via magnetic beads could be a solution.

While the SpyTag/SpyCatcher coupling improves the cell-electrode interface, it does not intrinsically increase the electron transfer rate of MtrC itself or address limitations in intracellular electron flux from metabolism to the outer membrane. These aspects would require complementary metabolic or protein engineering strategies. Several studies in this direction were conducted usually leading to an about two-fold increase in current density (Delgado et al., 2019; Sun et al., 2021).

While a variation in the batch-to-batch reproducibility of the SpyCatcher functionalization could be seen as further bottleneck, the consistency of results across five independent SpyCatcher functionalization experiments conducted in this study — using different batches of maleimide beads, gold beads, and gold electrodes — suggests that the functionalization protocol is sufficiently robust for repeated use, though a dedicated long-term stability assessment will be an important step toward practical device integration.

This study demonstrates a fast forward approach to screen for functional modifications of surface displayed enzymes. The MtrC-SpyTag can be implemented in already existing biosensors to improve the sensitivity and stability of these systems.

Funding

This work was supported by the Deutsche Forschungsgemeinschaft (priority program SPP2240, project no. 445800740 and priority program SPP2494, project no. 559358135).

CRediT authorship contribution statement

Lukas Kneuer: Conceptualization, Formal analysis, Investigation, Methodology, Visualization, Writing – original draft, Writing – review & editing. **René Wurst:** Investigation, Writing – review & editing. **Christian Jonas Lapp:** Formal analysis, Investigation, Methodology. **Nhật Quang Lê:** Investigation. **Leah Kobza:** Investigation. **Milena Menzel:** Investigation. **Edina Marlen Klein:** Investigation, Supervision. **Laura-Alina Philipp:** Conceptualization, Supervision, Writing – review & editing. **Catarina M. Paquete:** Conceptualization, Supervision, Writing – review & editing. **Johannes Gescher:** Conceptualization, Funding acquisition, Supervision, Writing – original draft, Writing – review & editing.

Declaration of competing interest

The authors declare that they have no competing interests.

Acknowledgements

We would like to thank Nils Grünke for his eager support in preparing the infrastructure for electrochemical measurements and Daniel Bauer for his highly appreciated help with the cell counting of microscopic images.

Figs. 1–4, S5, S7 and S8 were created using BioRender.com.

Appendix A. Supplementary data

Supplementary data to this article can be found online at https://doi.org/10.1016/j.bios.2026.118682.

Data availability

Data will be made available on request.

References

Abramson, J., Adler, J., Dunger, J., Evans, R., Green, T., Pritzel, A., Ronneberger, O., Willmore, L., Ballard, A.J., Bambrick, J., Bodenstein, S.W., Evans, D.A., Hung, C.C., O'Neill, M., Reiman, D., Tunyasuvunakool, K., Wu, Z., Žemgulytė, A., Arvaniti, E., Beattie, C., Bertolli, O., Bridgland, A., Cherepanov, A., Congreve, M., Cowen-Rivers, A.I., Cowie, A., Figurnov, M., Fuchs, F.B., Gladman, H., Jain, R., Khan, Y.A., Low, C.M.R., Perlin, K., Potapenko, A., Savy, P., Singh, S., Stecula, A., Thillaisundaram, A., Tong, C., Yakneen, S., Zhong, E.D., Zielinski, M., Žídek, A., Bapst, V., Kohli, P., Jaderberg, M., Hassabis, D., Jumper, J.M., 2024. Accurate structure prediction of biomolecular interactions with AlphaFold 3. Nature 630, 493–500. https://doi.org/10.1038/S41586-024-07487-W.

Bücking, C., Popp, F., Kerzenmacher, S., Gescher, J., 2010. Involvement and specificity of *Shewanella oneidensis* outer membrane cytochromes in the reduction of soluble and solid-phase terminal electron acceptors. FEMS Microbiol. Lett. 306, 144–151. https://doi.org/10.1111/J.1574-6968.2010.01949.X.

Cai, M., Ni, Z., Sun, Z., Li, X., Qi, Y., Wang, L., He, C., Li, C., 2025. The SpyTag/SpyCatcher system: precise regulation of covalent conjugation and expansion of application scenarios. Biotechnol. J. 20, e70131. https://doi.org/10.1002/biot.70131.

Carmona-Martinez, A.A., Harnisch, F., Fitzgerald, L.A., Biffinger, J.C., Ringeisen, B.R., Schröder, U., 2011. Cyclic voltammetric analysis of the electron transfer of

Shewanella oneidensis MR-1 and nanofilament and cytochrome knock-out mutants. Bioelectrochemistry 81, 74–80. https://doi.org/10.1016/j.bioelechem.2011.02.006.
Catania, C., Karbelkar, A.A., Furst, A.L., 2021. Engineering the interface between electroactive bacteria and electrodes. Joule 5, 743–747. https://doi.org/10.1016/j.joule.2021.02.001.
Chenani, H., Saeidi, M., Rastkhiz, M.S.A., Bolghanabadi, N., Aghaii, A.H., Orouji, M., Hatamie, A., Simchi, A., 2024. Challenges and advances of hydrogel-based wearable electrochemical biosensors for real-time monitoring of biofluids: from lab to market. A review. Anal. Chem. 96, 8160–8183. https://doi.org/10.1021/acs.analchem.3c03942.
Corts, A.D., Thomason, L.C., Gill, R.T., Gralnick, J.A., 2019. A new recombineering system for precise genome-editing in *Shewanella oneidensis* strain MR-1 using single-stranded oligonucleotides. Sci. Rep. 9, 39. https://doi.org/10.1038/s41598-018-37025-4.
Delgado, V.P., Paquete, C.M., Sturm, G., Gescher, J., 2019. Improvement of the electron transfer rate in *Shewanella oneidensis* MR-1 using a tailored periplasmic protein composition. Bioelectrochemistry 129, 18–25. https://doi.org/10.1016/j.bioelechem.2019.04.022.
Engel, C., Schattenberg, F., Dohnt, K., Schröder, U., Müller, S., Krull, R., 2019. Long-term behavior of defined mixed cultures of *Geobacter sulfurreducens* and *Shewanella oneidensis* in bioelectrochemical systems. Front. Bioeng. Biotechnol. 7. https://doi.org/10.3389/fbioe.2019.00060.
Flemming, H.C., van Hullebusch, E.D., Neu, T.R., Nielsen, P.H., Seviour, T., Stoodley, P., Wingender, J., Wuertz, S., 2023. The biofilm matrix: multitasking in a shared space. Nat. Rev. Microbiol. 21, 70–86. https://doi.org/10.1038/s41579-022-00791-0.
Flemming, H.-C., Wingender, J., 2010. The biofilm matrix. Nat. Rev. Microbiol. 8, 623–633. https://doi.org/10.1038/nrmicro2415.
Fourmond, V., 2016. QSoas: a versatile software for data analysis. Anal. Chem. 88, 5050–5052. https://doi.org/10.1021/acs.analchem.6b00224.
Gao, H., Barua, S., Liang, Y., Wu, L., Dong, Y., Reed, S., Chen, J., Culley, D., Kennedy, D., Yang, Y., He, Z., Nealson, K.H., Fredrickson, J.K., Tiedje, J.M., Romine, M., Zhou, J., 2010. Impacts of *Shewanella oneidensis* *c*-type cytochromes on aerobic and anaerobic respiration. Microb. Biotechnol. 3, 455–466. https://doi.org/10.1111/j.1751-7915.2010.00181.x.
Gao, W., Qiao, J., Hu, J., Guan, Y., Li, Q., 2024. Recent advances in intrinsically stretchable electronic materials and devices. Respons. Mater. 2, e20230022. https://doi.org/10.1002/rpm.20230022.
Golitsch, F., Bücking, C., Gescher, J., 2013. Proof of principle for an engineered microbial biosensor based on *Shewanella oneidensis* outer membrane protein complexes. Biosens. Bioelectron. 47, 285–291. https://doi.org/10.1016/j.bios.2013.03.010.
Goryshin, I.Y., Reznikoff, W.S., 1998. Tn5 *in vitro* transposition. J. Biol. Chem. 273, 7367–7374. https://doi.org/10.1074/jbc.273.13.7367.
Kiddee, P., Naidu, R., Wong, M.H., 2013. Electronic waste management approaches: an overview. Waste Manag. 33, 1237–1250. https://doi.org/10.1016/j.wasman.2013.01.006.
Klein, E., Wurst, R., Rehnlund, D., Gescher, J., 2024. Elucidating the development of cooperative anode-biofilm-structures. Biofilm 7, 100193. https://doi.org/10.1016/j.bioflm.2024.100193.
Knoll, M.T., Fuderer, E., Gescher, J., 2022. Sprayable biofilm – agarose hydrogels as 3D matrix for enhanced productivity in bioelectrochemical systems. Biofilm 4, 100077. https://doi.org/10.1016/j.bioflm.2022.100077.
Liu, G., 2021. Grand challenges in biosensors and biomolecular electronics. Front. Bioeng. Biotechnol. 9, 707615. https://doi.org/10.3389/fbioe.2021.707615.
Lockwood, C.W.J., Nash, B.W., Newton-Payne, S.E., van Wonderen, J.H., Whiting, K.P.S., Connolly, A., Sutton-Cook, A.L., Crook, A., Aithal, A.R., Edwards, M.J., Clarke, T.A., Sachdeva, A., Butt, J.N., 2024. Genetic code expansion in *Shewanella oneidensis* MR-1 allows site-specific incorporation of bioorthogonal functional groups into a *c*-Type cytochrome. ACS Synth. Biol. 13, 2833–2843. https://doi.org/10.1021/acssynbio.4c00248.
Lutz, Rolf, Hermann, Bujard, 1997. Independent and tight regulation of transcriptional units in *Escherichia coli* via the LacR/O, the TetR/O and AraC/I1-I2 regulatory elements. Nucleic Acids Res. 25, 1203–1210. https://doi.org/10.1093/nar/25.6.1203.
McCuskey, S.R., Su, Y., Leifert, D., Moreland, A.S., Bazan, G.C., 2020. Living bioelectrochemical composites. Adv. Mater. 32. https://doi.org/10.1002/adma.201908178.
Okamoto, A., Hashimoto, K., Nealson, K.H., Nakamura, R., 2013. Rate enhancement of bacterial extracellular electron transport involves bound flavin semiquinones. Proc. Natl. Acad. Sci. USA 110, 7856–7861. https://doi.org/10.1073/pnas.1220823110.
Paquete, C.M., Morgado, L., Salgueiro, C.A., Louro, R.O., 2022. Molecular mechanisms of microbial extracellular electron transfer: the importance of multiheme cytochromes. Front Biosci. (Landmark Ed.) 27, 174. https://doi.org/10.31083/j.fbl2706174.
Philipp, L.-A., Kneuer, L., Mayer-Windhorst, C., Jautelat, S., Le, N.Q., Gescher, J., 2025. Identification of factors limiting the efficiency of transplanting extracellular electron transfer chains in *Escherichia coli*. Appl. Environ. Microbiol. 91. https://doi.org/10.1128/aem.00685-25 e00685-25.
Reguera, G., McCarthy, K.D., Mehta, T., Nicoll, J.S., Tuominen, M.T., Lovley, D.R., 2005. Extracellular electron transfer via microbial nanowires. Nature 435, 1098–1101. https://doi.org/10.1038/nature03661.
Rivnay, J., Wang, H.-Y., Fenno, L., Deisseroth, K., Malliaras, G.G., 2017. Next-generation probes, particles, and proteins for neural interfacing. Sci. Adv. 3, e1601649. https://doi.org/10.1126/sciadv.1601649.
Rogers, J.A., Someya, T., Huang, Y., 2010. Materials and mechanics for stretchable electronics. Science 327, 1603–1607. https://doi.org/10.1126/science.1182383.
Roy, J.N., Babanova, S., Garcia, K.E., Cornejo, J., Ista, L.K., Atanassov, P., 2014. Catalytic biofilm formation by *Shewanella oneidensis* MR-1 and anode characterization by expanded uncertainty. Electrochim. Acta 126, 3–10. https://doi.org/10.1016/j.electacta.2013.07.075.
Roy, J.N., Garcia, K.E., Luckarift, H.R., Falase, A., Cornejo, J., Babanova, S., Schuler, A. J., Johnson, G.R., Atanassov, P.B., 2013. Applied electrode potential leads to *Shewanella oneidensis* MR-1 biofilms engaged in direct electron transfer. J. Electrochem. Soc. 160, H866–H871. https://doi.org/10.1149/2.001401jes.
Schindelin, J., Arganda-Carreras, I., Frise, E., Kaynig, V., Longair, M., Pietzsch, T., Preibisch, S., Rueden, C., Saalfeld, S., Schmid, B., Tinevez, J.-Y., White, D.J., Hartenstein, V., Eliceiri, K., Tomancak, P., Cardona, A., 2012. Fiji: an open-source platform for biological-image analysis. Nat. Methods 9, 676–682. https://doi.org/10.1038/nmeth.2019.
Schuetz, B., Schicklberger, M., Kuermann, J., Spormann, A.M., Gescher, J., 2009. Periplasmic electron transfer via the *c*-Type cytochromes MtrA and FccA of *Shewanella oneidensis* MR-1. Appl. Environ. Microbiol. 75, 7789–7796. https://doi.org/10.1128/AEM.01834-09.
Si, R.W., Zhai, D.D., Liao, Z.H., Gao, L., Yong, Y.C., 2015. A whole-cell electrochemical biosensing system based on bacterial inward electron flow for fumarate quantification. Biosens. Bioelectron. 68, 34–40. https://doi.org/10.1016/j.bios.2014.12.035.
Someya, T., Bao, Z., Malliaras, G.G., 2016. The rise of plastic bioelectronics. Nature 540, 379–385. https://doi.org/10.1038/nature21004.
Sun, W., Lin, Z., Yu, Q., Cheng, S., Gao, H., 2021. Promoting extracellular electron transfer of *Shewanella oneidensis* MR-1 by optimizing the periplasmic cytochrome *c* network. Front. Microbiol. 12, 727709. https://doi.org/10.3389/fmicb.2021.727709.
Webster, D.P., TerAvest, M.A., Doud, D.F.R., Chakravorty, A., Holmes, E.C., Radens, C. M., Sureka, S., Gralnick, J.A., Angenent, L.T., 2014. An arsenic-specific biosensor with genetically engineered *Shewanella oneidensis* in a bioelectrochemical system. Biosens. Bioelectron. 62, 320–324. https://doi.org/10.1016/j.bios.2014.07.003.
White, G.F., Shi, Z., Shi, L., Wang, Z., Dohnalkova, A.C., Marshall, M.J., Fredrickson, J.K., Zachara, J.M., Butt, J.N., Richardson, D.J., Clarke, T.A., 2013. Rapid electron exchange between surface-exposed bacterial cytochromes and Fe(III) minerals. Proc. Natl. Acad. Sci. U. S. A. 110, 6346–6351. https://doi.org/10.1073/pnas.1220074110.
Wurst, R., Klein, E., Gescher, J., 2024. Magnetic, conductive nanoparticles as building blocks for steerable micropillar-structured anodic biofilms. Biofilm 8, 100226. https://doi.org/10.1016/j.bioflm.2024.100226.
Xiao, Y., Zhang, E., Zhang, J., Dai, Y., Yang, Z., Christensen, H.E.M., Ulstrup, J., Zhao, F., 2017. Extracellular polymeric substances are transient media for microbial extracellular electron transfer. Sci. Adv. 3. https://doi.org/10.1126/sciadv.1700623.
Xu, S., Jangir, Y., El-Naggar, M.Y., 2016. Disentangling the roles of free and cytochrome-bound flavins in extracellular electron transport from *Shewanella oneidensis* MR-1. Electrochim. Acta 198, 49–55. https://doi.org/10.1016/j.electacta.2016.03.074.
Zajdel, T.J., Baruch, M., Méhes, G., Stavrinidou, E., Berggren, M., Maharbiz, M.M., Simon, D.T., Ajo-Franklin, C.M., 2018. PEDOT:PSS-based multilayer bacterial-composite films for bioelectronics. Sci. Rep. 8. https://doi.org/10.1038/s41598-018-33521-9.
Zakeri, B., Fierer, J.O., Celik, E., Chittock, E.C., Schwarz-Linek, U., Moy, V.T., Howarth, M., 2012. Peptide tag forming a rapid covalent bond to a protein, through engineering a bacterial adhesin. Proc. Natl. Acad. Sci. U. S. A. 109, E690–E697. https://doi.org/10.1073/pnas.1115485109.